Nanoscale Bouligand Multilayers

Hebing Hu, Sribharani Sekar, Wenbing Wu, Yann Battie, Vincent Lemaire, Oriol Arteaga, Lisa Poulikakos, David Norris, Harald Giessen, Gero Decher, et al.

Nanoscale Bouligand Multilayers: Giant Circular Dichroism of Helical Assemblies of Plasmonic 1D Nano-Objects

Hebing Hu, Sribharani Sekar, Wenbing Wu, Yann Battie, Vincent Lemaire, Oriol Arteaga, Lisa V. Poulikakos, David J. Norris, Harald Giessen, Gero Decher*, and Matthias Pauly

Abstract

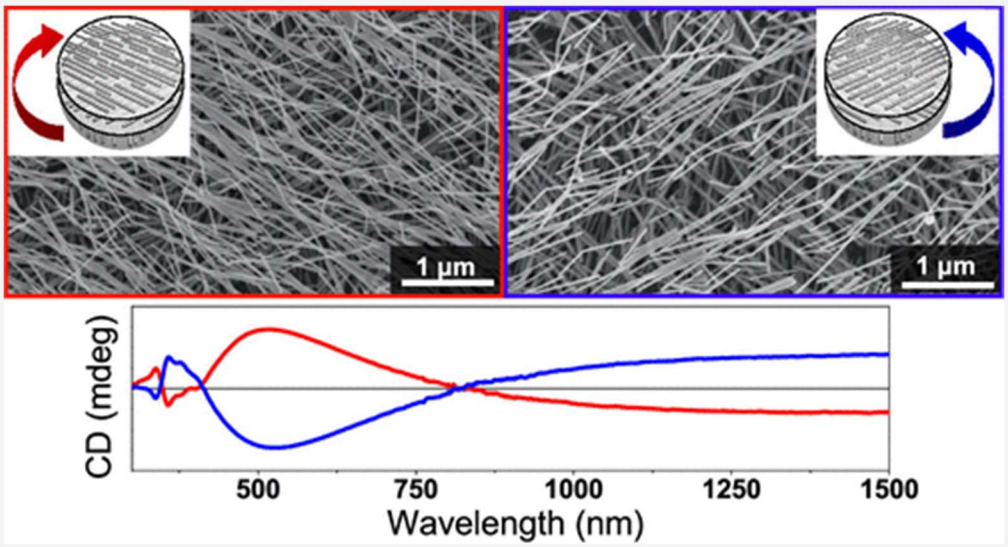

Chirality is found at all length scales in nature, and chiral metasurfaces have recently attracted attention due to their exceptional optical properties and their potential applications. Most of these metasurfaces are fabricated by top-down methods or bottom-up approaches that cannot be tuned in terms of structure and composition. By combining grazing incidence spraying of plasmonic nanowires and nanorods and Layer-by-Layer assembly, we show that nonchiral 1D nano-objects can be assembled into scalable chiral Bouligand nanostructures whose mesoscale anisotropy is controlled with simple macroscopic tools. Such multilayer helical assemblies of linearly oriented nanowires and nanorods display very high circular dichroism up to 13 000 mdeg and giant dissymmetry factors up to $g \approx 0.30$ over the entire visible and near-infrared range. The chiroptical properties of the chiral multilayer stack are successfully modeled using a transfer matrix formalism based on the experimentally determined properties of each individual layer. The proposed approach can be extended to much more elaborate architectures and gives access to template-free and enantiomerically pure nanocomposites whose structure can be finely tuned through simple design principles.

KEYWORDS:nanowire assemblies, chiral nanostructures, plasmonics, metasurfaces, circular dichroism

Chirality refers to the geometric property of any object lacking mirror planes or inversion symmetry and is found at all length scales in nature (1) ranging from macroscopic objects such as snails (2) or stem coiling of climbing plants (3) to the molecular scale, as in amino acids or proteins. (4) Synthetic methods for producing chiral materials are also scale-dependent: molecules are made by asymmetric

synthesis, (5) and mesoscale objects are frequently obtained through self-assembly (bottom-up) (6) or lithography-based (top-down) approaches. (7) Top-down techniques are typically used to make chiral plasmonic metasurfaces whose potential applications have led to a recent burst in research, (8) but they require complex fabrication technologies that are extremely costly and not scalable. Self-assembled inorganic chiral systems are a promising alternative, (9,10) but the associated chiroptical response is weaker and difficult to control, and self-assembled materials are also difficult to connect to the macroscopic world in any multiscale device.

Bouligand structures are composed of layers of unidirectionally aligned fiber-like objects progressively rotated with respect to the neighboring layers. (11) They offer the huge advantage that their base elements (1D objects) can be nonchiral and that chirality arises solely from the geometrical arrangement of the base elements in space. Some of these structures occur in nature and are responsible, for example, for extraordinary mechanical properties as in the dactyl club of Mantis shrimps. (12) They can also be produced artificially by techniques such as nanolithography, where they give rise to exceptional circular dichroism. (13)

Layer-by-Layer (LbL) assembly is well known for fabricating layered multimaterial nanocomposites, (14−16) and it has been recently demonstrated that it can be joined with grazing incidence spraying (GIS) to prepare multilayer assemblies of 1D nano-objects with unidirectional in-plane anisotropy. (17−21) The combination of GIS and LbL assembly meets all requirements for preparing scalable multimaterial Bouligand architectures; in this article we demonstrate that the alignment direction of each 1D nano-object layer in the multilayer stack is controlled independently and efficiently by macroscopic constraints (variation of spraying direction by in-plane sample rotation). Using this approach, scalable nanostructures are obtained whose tunable chiral meso- or nanoscale anisotropy is steered with simple macroscopic tools using entirely nonchiral building blocks. As an example, we report on the buildup of large-area chiral thin films of nonchiral silver nanowires and gold nanorods, leading to low-cost self-assembled plasmonic metasurfaces that display a giant broadband circular dichroism (CD), with, to the best of our knowledge, the largest CD values reported at the thinnest layer thickness for samples that can be easily fabricated at low cost over a cm^2 area.

These self-assembled Bouligand films compare in several aspects favorably to a group of chiral plasmonic nanomaterials (22,23) which have in recent years evolved into the field of metasurfaces (24) due to numerous potential applications, including sensing, (25) optical recording, (26) chiral mirrors, (27) and asymmetric second-harmonic generation (28) or as broadband circular polarizers. (29) Most of these inorganic metasurfaces are fabricated by top-down methods such as direct laser writing (30) or e-beam lithography, (13,31) which are not suited for macroscale device fabrication. Self-assembly of wet-synthesized, well-defined building blocks has thus been proposed as a promising approach toward large-scale production, (32−35) including for example using DNA origami. (36−40) Other strategies involve the chiral nanoscale arrangement of plasmonic nanoparticles by macroscopic deformation (41) or from a chiral template. (42−44) While a variety of methods have been proposed for the assembly of nanowires and nanorods in thin films with in-plane anisotropy, (45) they typically do not provide much versatility over the hierarchical architecture and composition of a multiscale material and thus lack the tunability of the desired structure-dependent materials properties. Hierarchical functional materials are anisotropic with respect to the materials composition,

morphology, and the complex directional anisotropies over several length scales, and their fabrication needs to be based on construction principles complying with these needs. While LbL assembly has been serving well for making countless layered nanocomposites, the approach proposed here gives access to template-free and enantiomerically pure chiral architectures. Since unidirectional or chiral “slabs” can freely be included in any position of a LbL multilayer stack, much more elaborate multimaterial nanocomposites with complex anisotropies that can be finely tuned at the nanoscale may be prepared using this approach.

Results and Discussion

The oriented assembly of nanowires or nanorods by GIS is based on the spraying of a suspension of the 1D nano-objects at a low angle on a transparent substrate coated with poly(ethylene imine) (PEI) (Figure 1A), which leads to the adsorption of an oriented sub-monolayer thin film of the 1D nano-objects at the substrate–water interface (Figure 1B). (18,20) Using this approach, highly oriented thin films of silver nanowires (46) (AgNWs, $d \approx 47 \pm 6$ nm, $L \approx 4.2 \pm 1.5$ μm) and gold nanorods (47) (AuNRs, $d \approx 15 \pm 3$ nm, $L \approx 245 \pm 50$ nm) can be obtained, with a 2D nematic order parameter as high as 0.79 for AgNWs (Figure 1C) and 0.45 for AuNRs with much smaller aspect ratios (Figure S3). The transmittance of linearly polarized light of those oriented thin films is highly anisotropic, as the longitudinal and transverse localized surface plasmon resonance modes are selectively excited depending on the direction of the light polarization (Figure S4). Following the anisotropic deposition of the first 1D nano-object layer, polyelectrolyte multilayers (PEMs) are formed through Layer-by-Layer assembly by successively spraying polycations (PEI or poly(allylamine hydrochloride), PAH) and polyanions (poly(styrenesulfonate), PSS). The sequence of polymers is expressed as PEM = PEI/(PSS/PAH)$_5$/PSS/PEI, and the thickness of such a polyelectrolyte multilayer is around 13 nm. A second nano-object layer may be placed on top of the PEM with the direction of orientation rotated by a freely selectable angle (here 60 degrees) with respect to the alignment direction of the first nano-object layer below (Figure 1D,E). Adding an additional PEM and nano-object layer completes a chiral three-layer helical assembly (Figure 1F,G). Depending on the sign of the rotation between the alignment directions of the oriented layers, left- (Figure 1D,F) or right-handed chiral metasurfaces are formed (Figure 1E,G). One advantage of this “directed self-assembly” approach is that such films are readily fabricated over large areas (Figure S5 shows the homogeneity of the thin films on several cm^2, which may potentially be scaled up to even larger surfaces by moving the spray nozzle over the substrate) at room temperature with simple equipment and starting from commercial polymers and previously synthesized 1D nano-objects.

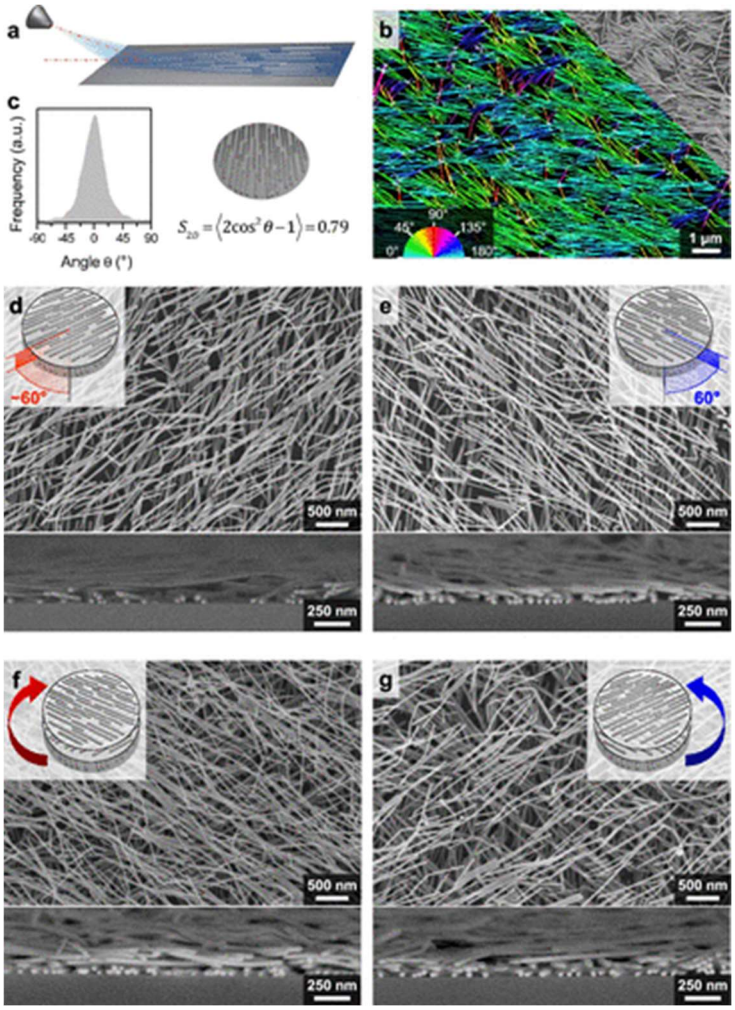

Figure 1. Assembly of Ag nanowires in Bouligand nanostructures. (a) Schematic of the spray-induced orientation of nanowires, (b) SEM of the resulting monolayer of oriented AgNWs color-coded according to their orientation, and (c) angular distribution of the AgNW orientation. (d–g) Top-view and cross-section SEM of two-layer (d, e) and three-layer (f, g) left-handed (d, f) and right-handed (e, g) AgNW thin films.

The optical properties of the one-, two-, and three-layer AgNW films are compared in Figure 2A for λ = 300–2000 nm (magnified spectra for λ = 300–800 nm are given in Figure S6). The extinction of the metasurface increases with the number of layers. The extinction spectrum of the AgNW metasurfaces displays peaks at 350 and 380 nm, which correspond to transverse modes of the localized surface plasmon resonance (LSPR) and a broad band starting at 600 nm and expanding into the near IR (NIR) which is arising from the longitudinal modes of the LSPR and reflection linked to the metallic character of the AgNW film in the NIR. When a second layer of AgNWs is added at −60° (left-handed, LH) or +60° (right-handed, RH), the films display a high CD signal (defined as the difference between the absorbance of left and right circularly polarized light), with a negative band close to the resonance wavelength of the transverse LSPR mode and a large positive band at λ > 460 nm for the LH sample. The enantiomer (RH sample) shows a perfectly symmetric spectrum, confirming that the observed CD is due to the chiral superstructure. The CD reaches a very high value of almost ±4000 mdeg at 380 nm for the two-layer metasurfaces.

When a third layer is added, the shape and the magnitude of the CD spectra are modified. The three-layer chiral superstructures made from AuNRs also display a very high CD with a different spectral shape than the AgNW metasurfaces as the longitudinal and transverse LSPR modes occur at different energies (Figure 2B). The CD of the LH film is slightly negative for λ < 500 nm; it displays a small positive peak at 550 nm and a broad and very intense peak centered at 850 nm, reaching values as high as +13 000 mdeg for the RH superstructure. Due to the symmetry of the sample, the sum of the linearly anisotropic optical properties of each individual layer is getting independent of the linear polarization of light and the transmittance of the three-layer thin films for linearly polarized light becomes almost independent from the orientation of the linear polarization (Figure S7).

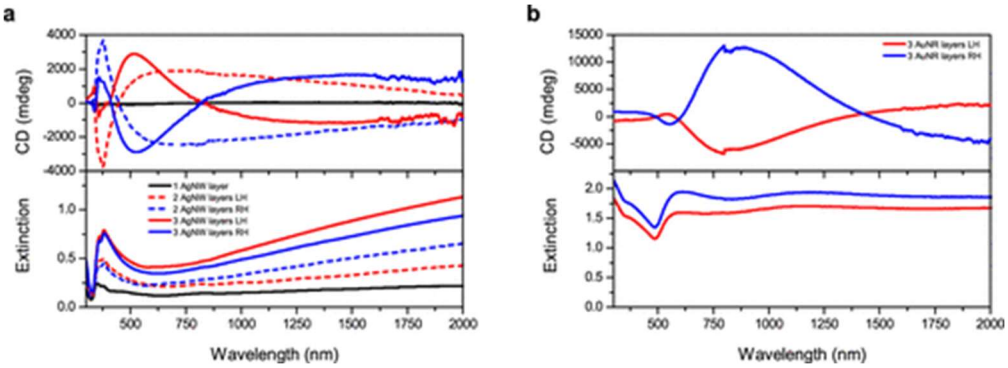

Figure 2. CD and extinction of the chiral metasurfaces. Measured broadband (300–2000 nm) CD and extinction spectra of (a) Ag nanowire and (b) Au nanorod chiral metasurfaces. For the AgNW thin films, the spectra measured after deposition of the first layer (black), second layer (dashed line), and third layer (full line) are given for the left-handed (LH, red) and right-handed (RH, blue) enantiomorphs.

The dimensionless Kuhn factor (the so-called *g*-factor (48)) was calculated from the ellipticity θ using eq 1 (the *g*-factor spectra are given in Figure S6):

$$g = \frac{\Delta A}{A} \approx \frac{4 \times \theta(\mathrm{rad})}{\ln 10 \times A} = \frac{4\pi \times \theta(\mathrm{mdeg})}{180 \times 1000 \times \ln 10 \times A} = \frac{\theta(\mathrm{mdeg})}{32982A} \quad (1)$$

The *g*-factor, which quantifies the chiroptical anisotropy, reaches an extremely high value of $g = 0.30$ at $\lambda = 650$ nm for the AgNW film and $g = 0.21$ at $\lambda = 850$ nm for the AuNR film, which is much higher than typical values obtained for chiral molecules (for examples, the *g*-factor of proteins is $\sim 10^{-3}$). Such giant *g*-factors have been predicted for chiral assemblies of plasmonic particles, (49) but the measured values of plasmonic chiral structures are usually 1 order of magnitude lower, (38,42,50,51) except for a very recent study in which a *g*-factor of 0.2 for gold nanorods with a chiral shape was reported. (52)

The chiral thin films consist of a helical stack of layers with a high linear anisotropy, and thus the optical properties of the chiral metasurfaces may be governed by the simultaneous influence of linear and circular dichroism as well as linear and circular birefringence. Therefore, the circular dichroism measured with a commercial CD spectrometer on such highly anisotropic thin films may be prone to artifacts. The optical properties have thus also been studied by Mueller matrix polarimetry (MMP), a technique that measures the 16 elements of the polarization transfer matrix (Figure S8 and Figure S9). (53) Indeed, the polarization state of light can be described by a four-element Stokes vector *S*. The Mueller matrix *M* is a 4 × 4 matrix that describes how a sample modifies the polarization state of the incoming light (described by S_{in}) to the outcoming Stokes vector $S_{out} = MS_{in}$. For a non-depolarizing sample, the

Mueller matrix can be related (eq 2) to the circular dichroism and birefringence, CD and CB, as well as the horizontal and 45° projections of linear dichroism (LD and LD′) and birefringence (LB and LB′):

$$M = \exp\begin{pmatrix} A & -\mathrm{LD} & -\mathrm{LD}' & \mathrm{CD} \\ -\mathrm{LD} & A & CB & \mathrm{LB}' \\ -\mathrm{LD}' & -\mathrm{CB} & A & -\mathrm{LB} \\ \mathrm{CD} & -\mathrm{LB}' & \mathrm{LB} & A \end{pmatrix} \quad (2)$$

The optical properties measured by MMP show that the chiral plasmonic metasurfaces give rise to a complex combination of circular and linear dichroism and birefringence and that CD, LD, CB, and LB are approximately of the same order of magnitude (Figure 3). The CD determined from MMP and by the commercial CD spectrometer are similar in shape and amplitude and are not changed when the sample is reversed (Figure S10). This is a key indication that the samples are truly chiral and we are not just measuring artifacts such as elliptical birefringence. (31,54) Furthermore, this demonstrates that despite a substantial linear dichroism, the CD spectra obtained by conventional CD spectrometry are indeed corroborated by MMP and that CD values of several thousand mdeg can be reached through the simple device fabrication described here.

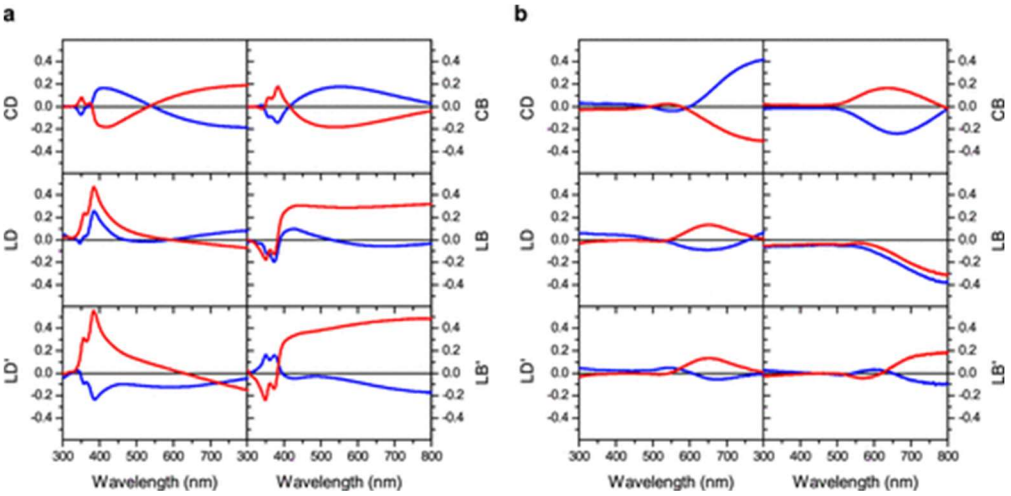

Figure 3. Optical properties of the chiral metasurfaces. Measured circular dichroism (CD), circular birefringence (CB), and horizontal and 45° projections of linear dichroism (LD and LD′) and of linear birefringence (LB and LB′) of (a) AgNW and (b) AuNR Bouligand assemblies obtained from the measured Mueller matrix.

Another tuning parameter for the chiroptical properties is the density of nanowires and nanorods in each oriented layer, which is controlled by the spraying time. (20)Figure S11 shows how the CD increases with increasing density of 1D nano-objects in each nano-object layer.

The optical properties of the AgNW chiral metasurfaces were modeled using a simple model based on a transfer matrix formalism (see Supporting Information). (55) The ordinary and extraordinary complex dielectric functions of a typical AgNW monolayer were fitted from ellipsometry spectra measured in reflection and were used to model the Mueller matrix of the two- and three-layer left- and right-handed chiral thin films (Figure S2). (56)Figure 4 indicates that the CD and CB deduced from the measured and modeled Mueller matrix are in good agreement. Although plasmon coupling is often invoked to explain the chiroptical properties of nanoparticle assemblies, we assume here that plasmonic coupling is not necessarily required to account for the

observed huge CD and CB values. Even a simple model composed of several independent linearly anisotropic layers that are helically twisted and separated by a dielectric spacer yields already high values for CD and CB. The slight differences between the modeling and our experiments are assumed to be due to morphological irregularities. While for the calculations the AgNW layers have been considered to be identical, the density and the quality of the in-plane orientation and confinement to the nanoscale object layers may vary in different layers.

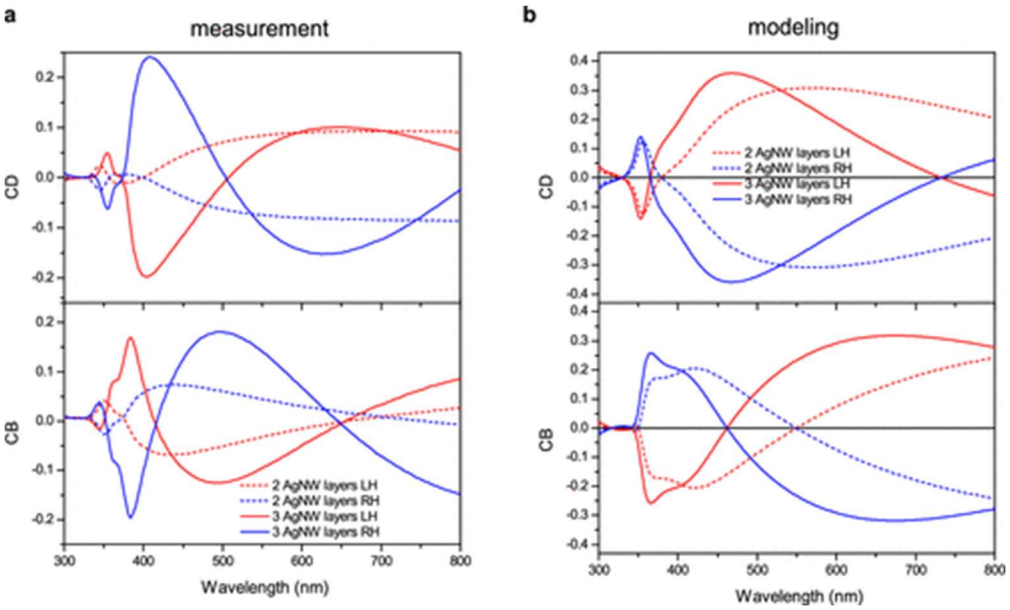

Figure 4. Modeling of the optical properties. Measured (a) and modeled (b) circular dichroism and circular birefringence of AgNW chiral metasurfaces. Fitting of the MMP of an oriented AgNW monolayer is used to retrieve the complex ordinary and extraordinary effective dielectric functions of a monolayer, which is used in a transfer matrix simulation (Berreman formalism) to model the MM of the left- and right-handed chiral metasurfaces (Figure S12). The measured CD and CB are calculated from the measured MMP (Figure S13).

Left- and right-handed two-layer samples oriented at ±45° were also characterized by chirality flux spectroscopy. The optical chirality flux (57,58) has been shown to be a physically useful observable that can be exploited as a far-field probe of local resonances at which one handedness dominates the chiral electromagnetic fields. In contrast to CD spectroscopy, which records the differential extinction of a sample upon excitation with left- and right-handed circularly polarized light, chirality flux spectroscopy probes the degree of circular polarization of light generated by a sample of interest. The sample is excited with monochromatic, linearly polarized light along the orientation of the bottom AgNW layer, while the degree of circular polarization of the scattered light is detected thanks to a photoelastic modulator, acting as a 50-kHz-modulated quarter-wave plate, a linear polarizer, oriented orthogonally to the incident linear polarizer, and a photomultiplier tube. Figure 5 shows that the chirality flux efficiency, a normalized form of the optical chirality flux (see Supporting Information), obtained for left- and right-handed samples, shown in red and blue, respectively, is clearly mirror-symmetric and shows a nearly perfect 100% generation of chiral light over the entire visible spectrum. In contrast, achiral samples (two nano-object layers oriented parallel or perpendicularly, shown in Figure 5 in black and green, respectively) generate a negligible chirality flux

efficiency, as expected. The Bouligand nanoarchitectures introduced here could therefore potentially serve as large-scale broadband generators of circularly polarized light.

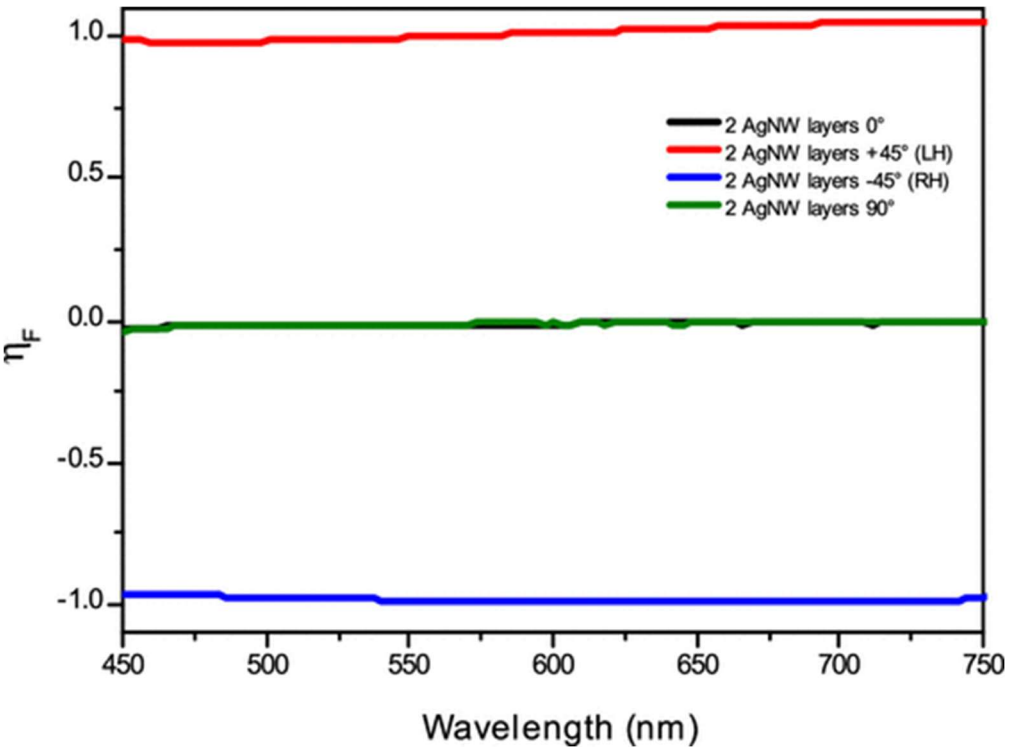

Figure 5. Measured chirality flux spectroscopy of two-layer AgNW chiral metasurfaces.

Conclusion

The layer-by-layer assembly of 1D nano-objects oriented by grazing incidence spraying into chiral Bouligand assemblies is shown to be a practical and efficient approach to fabricate chiral plasmonic metasurfaces over large areas. The direction of their nanoscale pitch and thus handedness is resulting from a simple sample rotation when spray depositing individual nanorod or nanowire layers. Such devices display highly anisotropic broadband chiroptical properties with giant dissymmetry factors that can be modeled fairly well using a simple transfer matrix approach. The chirality flux efficiency is close to 100% over the entire visible range. The chiral anisotropic properties are tunable by adjusting the in-plane density of the respective 1D nano-objects through the spraying time and the pitch of the helix through the twist angle of each nano-object layer and the thickness of the polyelectrolyte spacer layers. Note that further architectural variations are routinely accessible by placing additional components in other layers as desired or by adding more oriented nanowire and nanorod layers. Our work thus demonstrates that nanoscale multicomposites with designed anisotropies can now be obtained in a scalable way over macroscopic areas using simple equipment. Such plasmonic chiral thin films could serve as large-scale broadband generators of circularly polarized light across the entire visible range as demonstrated here, but this can probably be taken also to the near- and mid-IR and even THz range. The ease with which such nanostructures can be integrated to more complex devices also broadens their potential applications to sensing, for optical recording, or for chiral catalysis.

Nanocomposites with helical anisotropy are just one example demonstrating how this low-cost approach can be put to use on different surfaces ranging from foils to smooth macroscopic objects. It thus gives access to template-free chiral architectures whose structure can be finely tuned at the nanoscale using macroscopic tools and simple design rules, allowing the design of more elaborate multimaterial nanocomposites with complex anisotropies.

Materials and Methods

Materials

Poly(ethylenimine) ($\overline{M_n} \approx 60000$ g/mol)), poly(sodium 4-styrenesulfonate) ($\overline{M_w} \approx 70000$ g/mol), poly(allylamine hydrochloride) ($\overline{M_w} \approx 15000$ g/mol), polyvinylpyrrolidone (PVP, $\overline{M_w} \approx 40000$ g/mol), hexadecyltrimethylammonium bromide (CTAB H6269, >99.9%), hydrogen tetrachloroaurate trihydrate ($HAuCl_4 \cdot 3H_2O$, >99.9%), sodium borohydride ($NaBH_4$, >99%), L-ascorbic acid (>99%), silver nitrate ($AgNO_3$, >99%), and glycerol were purchased from Sigma-Aldrich, sodium chloride was purchased from Carl Roth, and nitric acid (68%) was purchased from Prolabo. The silver nanowires used for Figures 1, 2, 4, 5, S2, S4, S5, S6, and S13 were purchased from Novarials ($d \approx 55$ nm, $L \approx 23$ μm). All the chemicals were used without further purification. Silicon wafers were bought from WaferNet, and quartz and glass slides from Thuet B. Ultrapure water with a resistivity of 18.2 MΩ·cm was obtained by purification with a Milli-Q gradient system (Millipore) and was used directly after production. Poly(ethylene imine) solutions were freshly prepared by direct dissolution of 2.5 mg/mL of the polymer in ultrapure water. Poly(sodium 4-styrenesulfonate) solutions were prepared in NaCl solution (0.5 M) at a concentration of 0.618 mg/mL. Poly(allylamine hydrochloride) solutions were prepared in NaCl solution (0.5 M) at a concentration of 0.285 mg/mL.

Synthesis of Silver Nanowires

The AgNWs used for Figures 3, S7, S8, S10, and S11 were synthesized by a polyol reduction procedure previously reported in the literature. (46,59) A 1.76 g amount of PVP, $\overline{M_w} \approx 40000$ g/mol) was added into 57 mL of glycerol in a round-bottom flask, and the solution was kept at 90 °C under stirring until a homogeneous solution was obtained. After cooling to room temperature, 0.47 g of $AgNO_3$ was added to the solution. Then a NaCl solution (17.7 mg of NaCl dissolved in 0.15 mL of ultrapure water and 3 mL of glycerol) was added to the reaction mixture. The solution was heated from room temperature to 210 °C in 20 min while stirring. When the temperature reached 210 °C, the heating was stopped. A 60 mL amount of ultrapure water was added, and the solution left to return to room temperature. The solution was kept undisturbed for 1 week, and the sediment at the bottom of the flask was collected carefully. The obtained Ag nanowires were carefully washed 10–15 times with Milli-Q water by centrifugation at 2000 rpm for 30 min. Finally, the products were suspended in 170 mL of water. The resulting AgNWs have a cross-section of 47 ± 6 nm and a length of 4.2 ± 1.5 μm, as determined by transmission electron microscopy (TEM). The concentration was found to be 1.20 mg/mL by freeze-drying and weighing a known volume of suspension.

Synthesis of Gold Nanorods

AuNRs were synthesized by a typical three-step seed-mediated protocol adapted from Huang *etal*. (47) In brief, gold seeds were formed by a one-shot injection of freshly prepared 0.2 M $NaBH_4$ aqueous solution (450 μL) into a 10 mL solution of 0.1 M CTAB and 0.25 mM $HAuCl_4$ at 27 °C. Seed formation was indicated by a quick color change from yellow-orange to brown due to the complete reduction of Au^{3+} by $NaBH_4$. After 5 min of vigorous stirring, the CTAB-stabilized gold seeds were aged for 2 h without stirring.

Meanwhile, the so-called growth solution was prepared by introducing 25 mL of the 0.25 mM gold salt solution into 973 mL of 0.1 M CTAB. This solution was stirred for 15 min at 27 °C followed by addition of 2 mL of 1 mM HNO_3 in order to modify the pH. A 83 mL sample of this 1 L growth solution was added to flasks A and B, and the remaining 834 mL to flask C. Then 463 μL, 463 μL, and 4.63 mL of the freshly prepared 0.1 M ascorbic acid solution were added respectively to flasks A, B, and C. The solutions became clear upon gentle shaking, indicating the reduction of Au^{3+} to Au^{+}. Finally, 7.4 mL of the seed solution was added into flask A and shaken for 10 s. Then 7.4 mL of the solution from flask A was quickly added to flask B and shaken for 10 s. Then 74 mL of solution B was introduced into flask C and shaken for 30 s. Appearance of a purple color denotes the formation of gold nanoparticles, and this became darker with time and finally turned reddish-brown. Flask C was thermostated for 5 days at 27 °C. Eventually, the upper solution mostly containing gold nanoparticles was carefully pipetted out. The thin brown layer at the bottom of the flask was dispersed in 50 mL of water. The resulting dispersion was purified by centrifugation at 2000 rpm for 30 min twice to remove excess CTAB.

Surface Functionalization of AuNRs-CTAB

Attempts to form dense films of CTAB-coated gold nanorods on positively or negatively charged polyelectrolyte films were not successful, and thus ligand exchange with PVP was performed. A 50 mL amount of CTAB-stabilized gold nanorods was added dropwise to 500 mL of a 10 wt % PVP solution under ultrasonication followed by a gentle overnight stirring (150 rpm) at 27 °C. The PVP-coated AuNRs were centrifuged at 3000 rpm for 1 h to remove uncoated PVP. The purple precipitate present on the side walls of the tubes was redispersed in ethanol by brief sonication (30 s). The resulting brown solution was recentrifuged at the same condition to remove excess PVP if any and finally redispersed in water. The synthesized gold nanorods have a diameter of 15 ± 3 nm and a length of 245 ± 50 nm as determined from TEM images.

Oriented Deposition by Grazing Incidence Spraying

Silicon wafers and glass and quartz slides were cleaned thoroughly with ethanol and Milli-Q water. Prior to use, each substrate was activated for 3 min by plasma. For film buildup, the substrates were first orthogonally sprayed with the PEI solution for 10 s using Air-Boy spraying bottles followed by rinsing in pure water for 10 s.

AgNWs were deposited on the PEI-coated substrates for 200 s while the AuNRs were sprayed for 250 s. We used a homemade spraying system, which includes a gas flow controller to adjust the air flow rate (model Red-Y, Voegtlin), a liquid handling pump (model M50, VICI), and two-fluid nozzles (internal diameter: 300 μm, Spraying Systems). The liquid flow rate was set to 1 mL/min and the air flow to 30

L/min for the AgNWs and 40 L/min for the AuNRs. The angle between the spray cone main axis and the receiver substrate was 15°. The deposition was followed by a rinsing step with water for 100 s using an equivalent nozzle fed with air flow at 25 L/min and a water flow rate at 10 mL/min. The nozzle was held at a distance of 1 cm from the substrate. Finally, the substrates were dried using air flow.

For the chiral multilayer buildup, the first oriented layer of AgNWs or AuNRs was deposited on the PEI-coated quartz slide by grazing incidence spraying, followed by a polyelectrolyte multilayer of PEI/(PSS/PAH)$_5$/PSS/PEI. A second 1D nano-object layer can be deposited on top of the polyelectrolyte multilayer with the orientation direction shifted by a certain angle with respect to the direction of the underlying 1D nano-object direction. The same process can be repeated once more to form a chiral three-layer helical films. Depending on the sign of the angular shift between the oriented layers, left- or right-handed chiral metasurfaces are formed.

Electron Microscopy

TEM was performed at 200 kV with a Tecnai G2 (FEI) microscope and an Eagle 2 k (FEI) ssCCD camera. Cross-sections of the samples have been prepared with a Hitachi IM4000Plus ion milling system. A low-energy Ar^+ ion beam (6 keV) is used to produce a polished and undistorted cross-section without applying mechanical stress to the sample. The cross-section was observed using a FEG-SEM (Hitachi SU8010) at 1 keV. The images were taken with the SE-in lens detector.

UV–Vis and CD Spectroscopy

UV–vis spectra were recorded with a Cary5000 spectrophotometer equipped with a Glan-Taylor polarizer or with a depolarizer. The measurements were done through a 5 mm diameter circular hole. CD spectra were measured with Jasco J-1700 circular dichroism spectrometer equipped with a xenon arc lamp.

Mueller Matrix Polarimetry

Two different instruments have been used for the measurement of the Mueller matrix. A home-built Mueller matrix polarimeter that incorporates four photoelastic modulators (4-PEM polarimeter) (53) was used to determine, in transmission mode, the full Mueller matrix of the samples in the spectroscopic range from 250 to 800 nm in steps of 2 nm (Figure 3 and Figures S8, S9, and S10). A phase-modulated ellipsometer (UVISEL, Horiba) that measures the first three columns of the Mueller matrix in the 270 to 800 nm spectral range was also used (Figure 4 and Figures S12 and S13). The light spot had a diameter of 1.5 mm, and measurements were done in the central area of the samples. The obtained measurements were, in good approximation, not depolarizing, and they were analyzed according to eq 2.

Chirality Flux Spectroscopy

Chirality flux spectroscopy was performed as in Figure 5 using the experimental methodology introduced in previous work. (58) This method determines the chirality flux efficiency, defined as $\eta_{\bar{\mathcal{F}}} = \frac{c}{\omega P_{\text{tot}}}\bar{\mathcal{F}}$ (3) where c is the speed of light, ω is the angular frequency, and P_{tot} is the total power of the outgoing light. The integral of the optical chirality flux through a surface denoted as S is defined as $\bar{\mathcal{F}} = \int_S \text{Re}(\mathcal{F}\cdot n)dS$,

where $\mathcal{F} = \frac{1}{4}[\varepsilon \times (\nabla \times \mathcal{H}^*) - \mathcal{H}^* \times (\nabla \times \varepsilon)]$ is the optical chirality flux, ε is the complex electric field amplitude, and $\mathcal{H}$ is the complex magnetic field amplitude, while the asterisk denotes the complex conjugate.

Modeling

The Mueller matrix of nanostructures is simulated in transmission according to the Berreman transfer matrix formalism (BTM). (55) Three different structures with one, two, and three layers of AgNWs deposited on a transparent silica substrate are considered, as depicted in Scheme S1. The BTM formalism requires the knowledge of the dielectric function of each layer, which are deduced from ellipsometric measurements performed in reflection on films deposited on a silicon substrate. The dielectric constant of the organic layers is set to 2.34. The ordinary (ε_o) and extraordinary (ε_e) effective dielectric function of the aligned AgNW layer are shown in Figure S2. The linear or circular dichroism and birefringence are then calculated from the Mueller matrix by using the differential Mueller matrix decomposition. (56)

Acknowledgments

The authors wish to thank the electron microscopy platform of the Institute Charles Sadron for their help in the characterization of the multilayer samples, the ellipsometry core facility of LCP-A2MC (Université de Lorraine, http://lcp-a2mc.univ-lorraine.fr), and Thomas Hermans for giving access to his CD spectrometer at the initial stage of this project.

References

ARTICLE SECTIONS
Jump To

1. **1**

Hegstrom, R. A.; Kondepudi, D. K. The Handedness of the Universe. *Sci. Am.* **1990**, *262*, 108– 115, DOI: 10.1038/scientificamerican0190-108

[Crossref], Google Scholar

2. **2**

Kuroda, R.; Endo, B.; Abe, M.; Shimizu, M. Chiral Blastomere Arrangement Dictates Zygotic Left–Right Asymmetry Pathway in Snails. *Nature* **2009**, *462*, 790– 794, DOI: 10.1038/nature08597

[Crossref], [PubMed], [CAS], Google Scholar

3. **3**

Gerbode, S. J.; Puzey, J. R.; McCormick, A. G.; Mahadevan, L. How the Cucumber Tendril Coils and Overwinds. *Science* **2012**, *337*, 1087, DOI: 10.1126/science.1223304

[Crossref], [PubMed], [CAS], Google Scholar

4. **4**

Kelly, S. M.; Price, N. C. The Use of Circular Dichroism in the Investigation of Protein Structure and Function. *Curr. Protein Pept. Sci.* **2000**, *1*, 349– 384, DOI: 10.2174/1389203003381315

[Crossref], [PubMed], [CAS], Google Scholar

5. **5**

Brown, J. M.; Davies, S. G. Chemical Asymmetric Synthesis. *Nature* **1989**, *342*, 631– 636, DOI: 10.1038/342631a0

[Crossref], [CAS], Google Scholar

6. **6**

Liu, M.; Zhang, L.; Wang, T. Supramolecular Chirality in Self-Assembled Systems. *Chem. Rev.* **2015**, *115*, 7304– 7397, DOI: 10.1021/cr500671p

[ACS Full Text], [CAS], Google Scholar

7. **7**

Liu, N.; Hentschel, M.; Weiss, T.; Alivisatos, A. P.; Giessen, H. Three-Dimensional Plasmon Rulers. *Science* **2011**, *332*, 1407– 1410, DOI: 10.1126/science.1199958

[Crossref], [PubMed], [CAS], Google Scholar

8. **8**

Valev, V. K.; Baumberg, J. J.; Sibilia, C.; Verbiest, T. Chirality and Chiroptical Effects in Plasmonic Nanostructures: Fundamentals, Recent Progress, and Outlook. *Adv. Mater.* **2013**, *25*, 2517– 2534, DOI: 10.1002/adma.201205178

[Crossref], [PubMed], [CAS], Google Scholar

9. **9**

Ma, W.; Xu, L.; de Moura, A. F.; Wu, X.; Kuang, H.; Xu, C.; Kotov, N. A. Chiral Inorganic Nanostructures. *Chem. Rev.* **2017**, *117*, 8041– 8093, DOI: 10.1021/acs.chemrev.6b00755

[ACS Full Text], [CAS], Google Scholar

10. **10**

Hentschel, M.; Schäferling, M.; Duan, X.; Giessen, H.; Liu, N. Chiral Plasmonics. *Sci. Adv.* **2017**, 3, e1602735 DOI: 10.1126/sciadv.1602735 .

[Crossref], [PubMed], [CAS], Google Scholar

11. **11**

Bouligand, Y. Sur une Architecture Torsadée Répandue dans de Nombreuses Cuticules d'Arthropodes. *C. R. Acad. Sci.* **1965**, *261*, 3665– 3668

Google Scholar

12. **12**

Weaver, J. C.; Milliron, G. W.; Miserez, A.; Evans-Lutterodt, K.; Herrera, S.; Gallana, I.; Mershon, W. J.; Swanson, B.; Zavattieri, P.; DiMasi, E.; Kisailus, D. The Stomatopod Dactyl Club: A Formidable Damage-Tolerant Biological Hammer. *Science* **2012**, *336*, 1275, DOI: 10.1126/science.1218764

[Crossref], [PubMed], [CAS], Google Scholar

13. **13**

Zhao, Y.; Belkin, M. A.; Alù, A. Twisted Optical Metamaterials for Planarized Ultrathin Broadband Circular Polarizers. *Nat. Commun.* **2012**, *3*, 870, DOI: 10.1038/ncomms1877

[Crossref], [PubMed], [CAS], Google Scholar

14. **14**

Decher, G. Fuzzy Nanoassemblies: Toward Layered Polymeric Multicomposites. *Science* **1997**, *277*, 1232– 1237, DOI: 10.1126/science.277.5330.1232

[Crossref], [CAS], Google Scholar

15. **15**

Richardson, J. J.; Cui, J.; Björnmalm, M.; Braunger, J. A.; Ejima, H.; Caruso, F. Innovation in Layer-by-Layer Assembly. *Chem. Rev.* **2016**, *116*, 14828– 14867, DOI: 10.1021/acs.chemrev.6b00627

[ACS Full Text], [CAS], Google Scholar

16. **16**

Zhao, S.; Caruso, F.; Dähne, L.; Decher, G.; De Geest, B. G.; Fan, J.; Feliu, N.; Gogotsi, Y.; Hammond, P. T.; Hersam, M. C.; Khademhosseini, A.; Kotov, N.; Leporatti, S.; Li, Y.; Lisdat, F.; Liz-Marzán, L. M.; Moya, S.; Mulvaney, P.; Rogach, A. L.; Roy, S.The Future of Layer-by-Layer Assembly: A Tribute to ACS Nano Associate Editor Helmuth Möhwald. *ACS Nano* **2019**, *13*, 6151– 6169, DOI: 10.1021/acsnano.9b03326

[ACS Full Text], [CAS], Google Scholar

17. **17**

Blell, R.; Lin, X.; Lindström, T.; Ankerfors, M.; Pauly, M.; Felix, O.; Decher, G. Generating In-Plane Orientational Order in Multilayer Films Prepared by Spray-

Assisted Layer-by-Layer Assembly. *ACS Nano* **2017**, *11*, 84– 94, DOI: 10.1021/acsnano.6b04191

[ACS Full Text], [CAS], Google Scholar

18. **18**

Sekar, S.; Lemaire, V.; Hu, H.; Decher, G.; Pauly, M. Anisotropic Optical and Conductive Properties of Oriented 1D-Nanoparticle Thin Films made by Spray-Assisted Self-Assembly. *Faraday Discuss.* **2016**, *191*, 373– 389, DOI: 10.1039/C6FD00017G

[Crossref], [PubMed], [CAS], Google Scholar

19. **19**

Gao, J.; Wu, W.; Lemaire, V.; Carvalho, A.; Nlate, S.; Buffeteau, T.; Oda, R.; Battie, Y.; Pauly, M.; Pouget, E. Tuning the Chiroptical Properties of Elongated Nano-Objects *via* Hierarchical Organization. *ACS Nano* **2020**, *14*, 4111– 4121, DOI: 10.1021/acsnano.9b08823

[ACS Full Text], [CAS], Google Scholar

20. **20**

Hu, H.; Pauly, M.; Felix, O.; Decher, G. Spray-Assisted Alignment of Layer-by-Layer Assembled Silver Nanowires: A General Approach for the Preparation of Highly Anisotropic Nano-Composite Films. *Nanoscale* **2017**, *9*, 1307– 1314, DOI: 10.1039/C6NR08045F

[Crossref], [PubMed], [CAS], Google Scholar

21. **21**

Probst, P. T.; Sekar, S.; König, T. A. F.; Formanek, P.; Decher, G.; Fery, A.; Pauly, M. Highly Oriented Nanowire Thin Films with Anisotropic Optical Properties Driven by the Simultaneous Influence of Surface Templating and Shear Forces. *ACS Appl. Mater. Interfaces* **2018**, *10*, 3046– 3057, DOI: 10.1021/acsami.7b15042

[ACS Full Text], [CAS], Google Scholar

22. **22**

Fedotov, V. A.; Mladyonov, P. L.; Prosvirnin, S. L.; Rogacheva, A. V.; Chen, Y.; Zheludev, N. I. Asymmetric Propagation of Electromagnetic Waves through a Planar Chiral Structure. *Phys. Rev. Lett.* **2006**, *97*, 167401, DOI: 10.1103/PhysRevLett.97.167401

[Crossref], [PubMed], [CAS], Google Scholar

23. **23**

Fedotov, V. A.; Schwanecke, A. S.; Zheludev, N. I.; Khardikov, V. V.; Prosvirnin, S. L. Asymmetric Transmission of Light and Enantiomerically Sensitive Plasmon Resonance in Planar Chiral Nanostructures. *Nano Lett.* **2007**, *7*, 1996– 1999, DOI: 10.1021/nl0707961

[ACS Full Text], [CAS], Google Scholar

24. **24**

Plum, E.; Zhou, J.; Dong, J.; Fedotov, V. A.; Koschny, T.; Soukoulis, C. M.; Zheludev, N. I. Metamaterial with Negative Index Due to Chirality. *Phys. Rev. B: Condens. Matter Mater. Phys.* **2009**, *79*, 035407, DOI: 10.1103/PhysRevB.79.035407

[Crossref], [CAS], Google Scholar

25. **25**

Hendry, E.; Carpy, T.; Johnston, J.; Popland, M.; Mikhaylovskiy, R. V.; Lapthorn, A. J.; Kelly, S. M.; Barron, L. D.; Gadegaard, N.; Kadodwala, M. Ultrasensitive Detection and Characterization of Biomolecules Using Superchiral Fields. *Nat. Nanotechnol.* **2010**, *5*, 783– 787, DOI: 10.1038/nnano.2010.209

[Crossref], [PubMed], [CAS], Google Scholar

26. **26**

Zijlstra, P.; Chon, J. W. M.; Gu, M. Five-Dimensional Optical Recording Mediated by Surface Plasmons in Gold Nanorods. *Nature* **2009**, *459*, 410– 413, DOI: 10.1038/nature08053

[Crossref], [PubMed], [CAS], Google Scholar

27. **27**

Plum, E.; Zheludev, N. I. Chiral Mirrors. *Appl. Phys. Lett.* **2015**, *106*, 221901, DOI: 10.1063/1.4921969

[Crossref], [CAS], Google Scholar

28. **28**

Valev, V. K.; Silhanek, A. V.; Verellen, N.; Gillijns, W.; Van Dorpe, P.; Aktsipetrov, O. A.; Vandenbosch, G. A. E.; Moshchalkov, V. V.; Verbiest, T. Asymmetric Optical Second-Harmonic Generation from Chiral G-Shaped Gold Nanostructures. *Phys. Rev. Lett.* **2010**, *104*, 127401, DOI: 10.1103/PhysRevLett.104.127401

[Crossref], [PubMed], [CAS], Google Scholar

29. **29**

Gansel, J. K.; Thiel, M.; Rill, M. S.; Decker, M.; Bade, K.; Saile, V.; von Freymann, G.; Linden, S.; Wegener, M. Gold Helix Photonic Metamaterial as Broadband Circular Polarizer. *Science* **2009**, *325*, 1513– 1515, DOI: 10.1126/science.1177031

[Crossref], [PubMed], [CAS], Google Scholar

30. **30**

Ergin, T.; Stenger, N.; Brenner, P.; Pendry, J. B.; Wegener, M. Three-Dimensional Invisibility Cloak at Optical Wavelengths. *Science* **2010**, *328*, 337– 339, DOI: 10.1126/science.1186351

[Crossref], [PubMed], [CAS], Google Scholar

31. **31**

Hentschel, M.; Schäferling, M.; Weiss, T.; Liu, N.; Giessen, H. Three-Dimensional Chiral Plasmonic Oligomers. *Nano Lett.* **2012**, *12*, 2542– 2547, DOI: 10.1021/nl300769x

[ACS Full Text], [CAS], Google Scholar

32. **32**

Boles, M. A.; Engel, M.; Talapin, D. V. Self-Assembly of Colloidal Nanocrystals: From Intricate Structures to Functional Materials. *Chem. Rev.* **2016**, *116*, 11220– 11289, DOI: 10.1021/acs.chemrev.6b00196

[ACS Full Text], [CAS], Google Scholar

33. **33**

Mühlig, S.; Cunningham, A.; Dintinger, J.; Scharf, T.; Bürgi, T.; Lederer, F.; Rockstuhl, C. Self-Assembled Plasmonic Metamaterials. *Nanophotonics* **2013**, *2*, 211– 240, DOI: 10.1515/nanoph-2012-0036

[Crossref], [CAS], Google Scholar

34. **34**

Cecconello, A.; Besteiro, L. V.; Govorov, A. O.; Willner, I. Chiroplasmonic DNA-Based Nanostructures. *Nat. Rev. Mater.* **2017**, *2*, 17039, DOI: 10.1038/natrevmats.2017.39

[Crossref], [CAS], Google Scholar

35. **35**

Jiang, W.; Qu, Z.-b.; Kumar, P.; Vecchio, D.; Wang, Y.; Ma, Y.; Bahng, J. H.; Bernardino, K.; Gomes, W. R.; Colombari, F. M.; Lozada-Blanco, A.; Veksler, M.; Marino, E.; Simon, A.; Murray, C.; Muniz, S. R.; de Moura, A. F.; Kotov, N. A. Emergence of Complexity in Hierarchically Organized Chiral Particles. *Science* **2020**, *368*, 642, DOI: 10.1126/science.aaz7949

[Crossref], [PubMed], [CAS], Google Scholar

36. **36**

Kuzyk, A.; Schreiber, R.; Fan, Z.; Pardatscher, G.; Roller, E.-M.; Hogele, A.; Simmel, F. C.; Govorov, A. O.; Liedl, T. DNA-Based Self-Assembly of Chiral Plasmonic Nanostructures with Tailored Optical Response. *Nature* **2012**, *483*, 311– 314, DOI: 10.1038/nature10889

[Crossref], [PubMed], [CAS], Google Scholar

37. **37**

Shen, X.; Song, C.; Wang, J.; Shi, D.; Wang, Z.; Liu, N.; Ding, B. Rolling up Gold Nanoparticle-Dressed DNA Origami into Three-Dimensional Plasmonic Chiral Nanostructures. *J. Am. Chem. Soc.* **2012**, *134*, 146– 149, DOI: 10.1021/ja209861x

[ACS Full Text], [CAS], Google Scholar

38. **38**

Lan, X.; Lu, X.; Shen, C.; Ke, Y.; Ni, W.; Wang, Q. Au Nanorod Helical Superstructures with Designed Chirality. *J. Am. Chem. Soc.* **2015**, *137*, 457– 462, DOI: 10.1021/ja511333q

[ACS Full Text], [CAS], Google Scholar

39. **39**

Chen, Z.; Lan, X.; Chiu, Y.-C.; Lu, X.; Ni, W.; Gao, H.; Wang, Q. Strong Chiroptical Activities in Gold Nanorod Dimers Assembled Using DNA Origami Templates. *ACS Photonics* **2015**, *2*, 392– 397, DOI: 10.1021/ph500434f

[ACS Full Text], [CAS], Google Scholar

40. **40**

Kuzyk, A.; Urban, M. J.; Idili, A.; Ricci, F.; Liu, N. Selective Control of Reconfigurable Chiral Plasmonic Metamolecules. *Sci. Adv.* **2017**, 3, e1602803 DOI: 10.1126/sciadv.1602803 .

[Crossref], [PubMed], [CAS], Google Scholar

41. **41**

Kim, Y.; Yeom, B.; Arteaga, O.; Jo Yoo, S.; Lee, S.-G.; Kim, J.-G.; Kotov, N. A. Reconfigurable Chiroptical Nanocomposites with Chirality Transfer from the Macro- to the Nanoscale. *Nat. Mater.* **2016**, *15*, 461– 468, DOI: 10.1038/nmat4525

[Crossref], [PubMed], [CAS], Google Scholar

42. **42**

Guerrero-Martínez, A.; Auguié, B.; Alonso-Gómez, J. L.; Džolić, Z.; Gómez-Graña, S.; Žinić, M.; Cid, M. M.; Liz-Marzán, L. M. Intense Optical Activity from Three-Dimensional Chiral Ordering of Plasmonic Nanoantennas. *Angew. Chem., Int. Ed.* **2011**, *50*, 5499– 5503, DOI: 10.1002/anie.201007536

[Crossref], [CAS], Google Scholar

43. **43**

Querejeta-Fernández, A.; Chauve, G.; Methot, M.; Bouchard, J.; Kumacheva, E. Chiral Plasmonic Films Formed by Gold Nanorods and Cellulose Nanocrystals. *J. Am. Chem. Soc.* **2014**, *136*, 4788– 4793, DOI: 10.1021/ja501642p

[ACS Full Text], [CAS], Google Scholar

44. **44**

Cheng, J.; Le Saux, G.; Gao, J.; Buffeteau, T.; Battie, Y.; Barois, P.; Ponsinet, V.; Delville, M.-H.; Ersen, O.; Pouget, E.; Oda, R. GoldHelix: Gold Nanoparticles Forming 3D Helical Superstructures with Controlled Morphology and Strong Chiroptical Property. *ACS Nano* **2017**, *11*, 3806, DOI: 10.1021/acsnano.6b08723

[ACS Full Text], [CAS], Google Scholar

45. **45**

Hu, H.; Wang, S.; Feng, X.; Pauly, M.; Decher, G.; Long, Y. In-Plane Aligned Assemblies of 1D-Nanoobjects: Recent Approaches and Applications. *Chem. Soc. Rev.* **2020**, *49*, 509– 553, DOI: 10.1039/C9CS00382G

[Crossref], [PubMed], [CAS], Google Scholar

46. **46**

Liu, J.-W.; Wang, J.-L.; Huang, W.-R.; Yu, L.; Ren, X.-F.; Wen, W.-C.; Yu, S.-H. Ordering Ag Nanowire Arrays by a Glass Capillary: A Portable, Reusable and Durable SERS Substrate. *Sci. Rep.* **2012**, *2*, 987, DOI: 10.1038/srep00987

[Crossref], [PubMed], [CAS], Google Scholar

47. **47**

Wang, Y.-N.; Wei, W.-T.; Yang, C.-W.; Huang, M. H. Seed-Mediated Growth of Ultralong Gold Nanorods and Nanowires with a Wide Range of Length Tunability. *Langmuir* **2013**, *29*, 10491– 10497, DOI: 10.1021/la400985n

[ACS Full Text], [CAS], Google Scholar

48. **48**

Berova, N.; Nakanishi, K.; Woody, R. W. *Circular Dichroism: Principles and Applications*; John Wiley & Sons: New York, USA, 2000; p 912.

Google Scholar

49. **49**

Liu, T.; Besteiro, L. V.; Liedl, T.; Correa-Duarte, M. A.; Wang, Z.; Govorov, A. O. Chiral Plasmonic Nanocrystals for Generation of Hot Electrons: Toward Polarization-Sensitive Photochemistry. *Nano Lett.* **2019**, *19*, 1395– 1407, DOI: 10.1021/acs.nanolett.8b05179

[ACS Full Text], [CAS], Google Scholar

50. **50**

Hu, T.; Isaacoff, B. P.; Bahng, J. H.; Hao, C.; Zhou, Y.; Zhu, J.; Li, X.; Wang, Z.; Liu, S.; Xu, C.; Biteen, J. S.; Kotov, N. A. Self-Organization of Plasmonic and Excitonic Nanoparticles into Resonant Chiral Supraparticle Assemblies. *Nano Lett.* **2014**, *14*, 6799– 6810, DOI: 10.1021/nl502237f

[ACS Full Text], [CAS], Google Scholar

51. **51**

Yan, W.; Xu, L.; Xu, C.; Ma, W.; Kuang, H.; Wang, L.; Kotov, N. A. Self-Assembly of Chiral Nanoparticle Pyramids with Strong R/S Optical Activity. *J. Am. Chem. Soc.* **2012**, *134*, 15114– 15121, DOI: 10.1021/ja3066336

[ACS Full Text], [CAS], Google Scholar

52. **52**

González-Rubio, G.; Mosquera, J.; Kumar, V.; Pedrazo-Tardajos, A.; Llombart, P.; Solís, D. M.; Lobato, I.; Noya, E. G.; Guerrero-Martínez, A.; Taboada, J. M.; Obelleiro, F.; MacDowell, L. G.; Bals, S.; Liz-Marzán, L. M. Micelle-Directed Chiral Seeded Growth on Anisotropic Gold Nanocrystals. *Science* **2020**, *368*, 1472, DOI: 10.1126/science.aba0980

[Crossref], [PubMed], [CAS], Google Scholar

53. **53**

Arteaga, O.; Freudenthal, J.; Wang, B.; Kahr, B. Mueller Matrix Polarimetry with Four Photoelastic Modulators: Theory and Calibration. *Appl. Opt.* **2012**, *51*, 6805– 6817, DOI: 10.1364/AO.51.006805

[Crossref], [PubMed], [CAS], Google Scholar

54. **54**

Frank, B.; Yin, X.; Schäferling, M.; Zhao, J.; Hein, S. M.; Braun, P. V.; Giessen, H. Large-Area 3D Chiral Plasmonic Structures. *ACS Nano* **2013**, *7*, 6321– 6329, DOI: 10.1021/nn402370x

[ACS Full Text], [CAS], Google Scholar

55. **55**

Schubert, M. Polarization-Dependent Optical Parameters of Arbitrarily Anisotropic Homogeneous Layered Systems. *Phys. Rev. B: Condens. Matter Mater. Phys.* **1996**, *53*, 4265– 4274, DOI: 10.1103/PhysRevB.53.4265

[Crossref], Google Scholar

56. **56**

Pérez, J. J. G.; Ossikovski, R. *Polarized Light and the Mueller Matrix Approach*; CRC Press, Taylor & Francis Group: Boca Raton, USA, 2016; p 405.

Google Scholar

57. **57**

Poulikakos, L. V.; Gutsche, P.; McPeak, K. M.; Burger, S.; Niegemann, J.; Hafner, C.; Norris, D. J. Optical Chirality Flux as a Useful Far-Field Probe of Chiral Near Fields. *ACS Photonics* **2016**, *3*, 1619, DOI: 10.1021/acsphotonics.6b00201

[ACS Full Text], [CAS], Google Scholar

58. **58**

Poulikakos, L. V.; Thureja, P.; Stollmann, A.; De Leo, E.; Norris, D. J. Chiral Light Design and Detection Inspired by Optical Antenna Theory. *Nano Lett.* **2018**, *18*, 4633– 4640, DOI: 10.1021/acs.nanolett.8b00083

[ACS Full Text], [CAS], Google Scholar

59. **59**

Yang, C.; Gu, H.; Lin, W.; Yuen, M. M.; Wong, C. P.; Xiong, M.; Gao, B. Silver Nanowires: From Scalable Synthesis to Recyclable Foldable Electronics. *Adv. Mater.* **2011**, *23*, 3052– 3056, DOI: 10.1002/adma.201100530
[Crossref], [PubMed], [CAS], Google Scholar

Cited By